MATERIALS SCIENCE

Laser vibrational excitation of radicals to prevent crystallinity degradation caused by boron doping in diamond

L. Fan[1]*, L. Constantin[1,2]*, Z. P. Wu[1], K. A. McElveen[3], X. G. Chen[4], T. He[5], F. Wang[6], C. Debiemme-Chouvy[7], B. Cui[6], R. Y. Lai[3], X. Li[5], J. F. Silvain[2], Y. F. Lu[1]†

Pursuing high-level doping without deteriorating crystallinity is prohibitively difficult but scientifically crucial to unleashing the hidden power of materials. This study demonstrates an effective route for maintaining lattice integrity during the combustion chemical vapor deposition of highly conductive boron-doped diamonds (BDDs) through laser vibrational excitation of a growth-critical radical, boron dihydride (BH_2). The improved diamond crystallinity is attributed to a laser-enabled, thermal nonequilibrium suppression of the relative abundance of boron hydrides (BH), whose excessive presence induces boron segregation and disturbs the crystallization. The BDDs show a boron concentration of 4.3×10^{21} cm^{-3}, a film resistivity of 28.1 milliohm·cm, and hole mobility of 55.6 cm^2 V^{-1} s^{-1}, outperforming a commercial BDD. The highly conductive and crystalline BDDs exhibit enhanced efficiency in sensing glucose, confirming the advantages of laser excitation in producing high-performance BDD sensors. Regaining crystallinity with laser excitation in doping process could remove the long-standing bottlenecks in semiconductor industry.

INTRODUCTION

In semiconductor physics and microelectronics, doping is a fundamental process enabling property tailoring and device fabrication. In situ doping is primarily used to grow bulk crystals with a homogenous doping profile and a controllable density but suffers from severe crystallinity degradation in a high-level doping regime (*1*, *2*). Pursuing high-level impurity doping without deteriorating crystallinity is prohibitively difficult, especially in materials with a rigid crystal structure like diamonds, but is scientifically crucial to unleashing unrealized device performance. Impurities introduced during the in situ doping process disturb the gas-phase reactions at chemical equilibrium, thus reducing the crystal phase stability and subsequently causing severe crystallinity degradation. Experimental indications show that deviation of the gas-phase reactions from the ideal growth condition detrimentally affects the crystal integrity during the in situ doping process (*1*–*3*).

Optimization of crystallization during the in situ doping is commonly practiced by varying external conditions, such as temperature or pressure (*4*, *5*). This stage of doping control relies on chemical reactions under thermodynamic equilibrium where energy is evenly and randomly distributed in the system. In other words, the doping is controlled only on an average "macroscopic" level. However, the way that energy is coupled into the system affects the reaction dynamics and, hence, the reaction outcome (*6*–*9*). A more delicate approach to control should involve an active intervention during doping. As coherent, monochromatic light sources with high radiation energy, lasers provide a unique means of directionally coupling energy into selected reactant molecules in the form of excitation of a specific vibrational degree of the reactant. With the help of laser vibrational excitation of selected molecules, the reacting system enters a thermal "nonequilibrium" state, which is inaccessible when energy is supplied in the form of heat (*6*). Accessing such a state allows us to exert "microscopic" control beyond traditional means, making it possible to distinguish the effects of different reacting channels on doping and crystallization.

Extensive experiments have shown that product pathways can be changed by selectively exciting certain molecules with laser irradiation (*9*–*13*). Crim (*8*) found that the products of thermal hydrogen (H) atoms with deuterium hydrogen oxide (HDO) prepared with different vibrational states are different. Yan *et al.* (*9*) reported that vibrational excitations have a strong impact on product states in the reaction of chlorine (Cl) and CHD_3. de Hemptinne *et al.* revealed that mode-selective ethylene chemistry influenced the energy transfer rates from the resonant modes (ν_7 and ν_{10}) to the chemical exit channel (ν_4) of ethylene (*10*). Nevertheless, laser chemical control studies have been focused on simple molecular reactions for a long time because of limited choices and high cost of laser sources. The increasing versatility of laser sources and their notably reduced operational cost make it possible to envision their enormous potential for enabling a control in practical applications (*11*–*14*).

In this work, taking boron-doped diamond (BDD) as a representative system, we demonstrated that laser vibrational excitation of the growth-critical radical, boron dihydride (BH_2), influences the flame chemistry in a thermal nonequilibrium way, leading to fast growth of highly conductive and crystalline BDDs. Diamond is electrically insulating in nature because of its wide bandgap of 5.5 eV. Exploiting diamonds for electronics, biosensing, and electrochemical applications relies on advances in doping techniques (*15*). However, diamond is ultrastable and chemically inert to most

[1]Department of Electrical and Computer Engineering, University of Nebraska-Lincoln, Lincoln, NE 68588, USA. [2]The French National Centre for Scientific Research, CNRS, University of Bordeaux, Bordeaux INP, ICMCB UMR 5026, F-33608 Pessac, France. [3]Department of Chemistry, University of Nebraska-Lincoln, Lincoln, NE 68588, USA. [4]Department of Physics and Astronomy, University of Nebraska-Lincoln, Lincoln, NE 68588, USA. [5]Department of Civil and Environmental Engineering, University of Nebraska-Lincoln, Lincoln, NE 68588, USA. [6]Department of Mechanical and Materials Engineering, University of Nebraska-Lincoln, Lincoln, NE 68588, USA. [7]Laboratoire Interfaces et Systémes Electrochimiques, UMR 8235, CNRS, Sorbonne Université, F-75252 Paris Cedex, France.
*These authors contributed equally to this work.
†Corresponding author. Email: ylu2@unl.edu

reactive reagents because of the strong σ-bonding formed between adjacent carbon atoms, making high-level substitutional doping very difficult. Boron (B) is currently the most successful dopant for producing p-type diamonds (*16*). However, B doping in diamonds by chemical vapor deposition (CVD) leads to severely degraded crystallinity at a high-level doping regime, making it difficult to achieve high electrical conductivity and crystallinity in BDDs (*17*, *18*). Figure 1 (A and B) schematically shows the perceived role of laser vibrational excitation of BH_2 in overcoming growth and incorporation limitations for B doping in diamonds. In situ doping proceeded with the addition of a certain amount of B-containing molecules into the diamond-forming oxyacetylene flame. By matching the laser wavelength to the fundamental vibrational quanta of BH_2, intentional control of the flame chemistry was realized.

Morphological observations and structural analysis of the BDDs prepared with laser vibrational excitation of BH_2 evidenced a substantial improvement of diamond crystallinity without sacrificing the conductivities. As shown in Fig. 1C, glucose sensing tests were performed to evaluate the functionality of the BDD electrodes prepared and their relationship with the vibrational excitation. A growth rate of 35 μm/hour was achieved, which is 30 to 100 times faster than hot filament CVD (HFCVD). The BDD electrodes were prepared using an open-air combustion CVD method with a nontoxic B source, boron acid, making BDD fabrication safe compared to HFCVD in which toxic diborane (B_2H_6) was usually used as the B source. Laser-enabled control of crystallization during the in situ doping process allows an in-depth understanding of the relationship between doping and crystal growth, thus holding great promise in removing the long-standing bottleneck in the semiconductor industry.

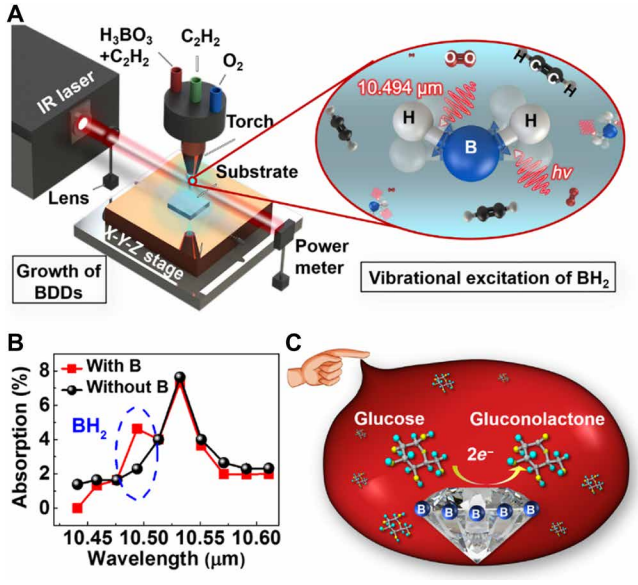

Fig. 1. Fabrication of highly conductive, crystalline BDDs with laser vibrational excitation toward high-performance sensors. (**A**) Schematic illustration of combustion CVD of BDDs, where BDDs grow at the proximity of the flame inner core and a laser beam with a wavelength of 10.494 μm irradiates the flame parallel to the substrate to resonantly excite the BH bending mode of BH_2. (**B**) The absorption spectrum of the laser energy within the laser emission spectrum range by a B-added oxyacetylene flame. (**C**) Glucose sensing test of the BDD electrodes to evaluate the role of laser vibrational excitation in producing high-performance BDD sensors. IR, infrared.

RESULTS

Effects of B doping on the BDD growth

As shown in scanning electron microscopy (SEM) micrographs of BDD films (Fig. 2A), the surface morphology of the films exhibits a strong dependence on the flow rate of the channel containing the B source (termed the B flow rate below). The grain size versus B flow rate plot (Fig. 2B) shows an increase first and then a sharp drop in the grain size upon the addition of B. The undoped diamond film has an average grain size of ~1.5 μm. Increasing the B flow rate from 0 to 40 standard cubic centimeters per minute (sccm) results in ~4-μm diamond grains with distinct growth steps on the surface. Increase in diamond grain size at low B doping levels was also observed in HFCVD and microwave plasma–enhanced CVD (MPCVD), which is caused by a catalyzing effect of B addition on the gas-phase reactions (*16*, *19*, *20*). As shown in the Raman spectra (Fig. 2C), up to 40 sccm, the films are dominated by a sharp diamond peak at ~1332 cm^{-1} and a weak G band (~1500 cm^{-1}) ascribed to graphitic carbon.

However, as the B flow rate increases from 60 to 80 sccm, diamond grains (Fig. 2A) decrease in size and the growth steps on the diamond grains become indistinguishable, suggesting that the crystalline quality turn out to be poor for high doping levels. The diamond peak of the BDD film prepared with a B flow rate of 60 sccm deforms asymmetrically, decreases in intensity, and widens with a downshift in its wave number. The asymmetrical deformation of the diamond peak upon the B addition is ascribed to a quantum Fano interference between the discrete zone-center phonon and a continuum of electronic states induced by B doping (*21*). The Raman spectra change markedly for the BDD prepared at a B flow rate of 80 sccm. The diamond peak appears only as a shoulder on a wide signal (300 to 1300 cm^{-1}) with maximums around 500 and 1200 cm^{-1}. The wide signal (300 to 1300 cm^{-1}) has been connected to intraband optical transitions due to the interference of the phonon and the

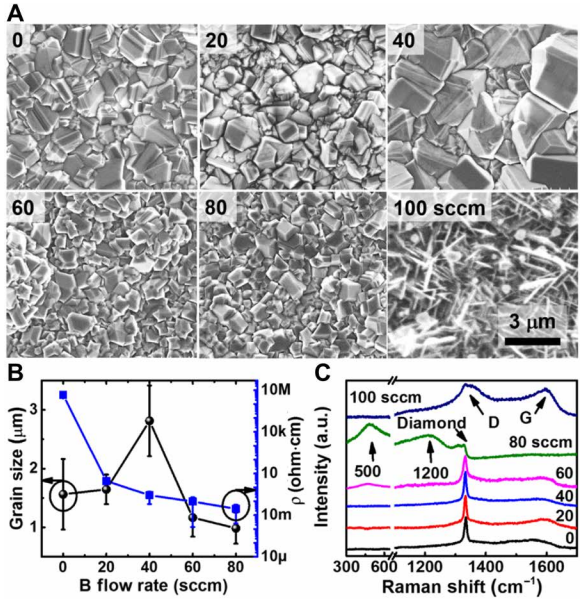

Fig. 2. Growth of BDDs with respect to the B flow rate. (**A**) In-plan SEM micrographs of BDDs prepared with different B flow rates. (**B**) The grain size and the film resistivity plotted as a function of the B flow rate. (**C**) Raman spectra of BDDs prepared with different B flow rates. a.u., arbitrary units.

impurity band–induced electronic state and normally occurs at a B density beyond 5×10^{20} cm^{-3} (*22*, *23*). At an extremely high B flow rate larger than 100 sccm, needle-like features appear in the BDD film, matching the observations in HFCVD and MPCVD (*17*, *20*). Its Raman spectrum shows dominant D (1360 cm^{-1}) and G bands (1590 cm^{-1}) associated with a weak diamond signature peak due to the substantial presence of disordered and graphitic carbon. The reduction in grain size and the emerging crystal imperfection at high doping levels suggests that the presence of excessive B-containing molecules in the reactive oxyacetylene flame triggers the onset of graphite formation and degrades the diamond crystalline quality.

The closely packed diamond lattice makes substitutional doping a challenging task. Both the thermodynamic and kinetic aspects of the diamond growth process can be severely affected by the introduction of a B-containing source (*19*). The presence of excessive B atoms in the reactive gases can progressively induce segregation of B clusters. The loss of the crystallinity at high doping levels can be attributed to the segregation of B clusters at the growing steps due to interstitial incorporation of B that disrupts the crystallization and induces secondary nucleation (*23*).

The resistivity of the BDD films prepared at different B flow rates is plotted in Fig. 2B. There is a marked drop of seven orders of magnitude in the film resistivity from 4.6 megohm·cm for the undoped film down to 0.2 ohm·cm for the heavily doped BDD film prepared at a B flow rate of 80 sccm, confirming effective doping and metallic-type conductivity.

Effects of laser vibrational excitation of BH_2 on the BDD growth

The absorption spectrum of the infrared (IR) laser energy by the combustion flame with and without the addition of B is presented in Fig. 1B. Note that, because of a trace amount of B source in the flame, no obvious absorption was detected with a simple oxyacetylene flame. A small amount of ethylene was, therefore, added into the flame to enhance the absorption sensitivity. Within the available emission spectrum range of the IR laser, the peak, at 10.532 μm, in the absorption spectra results from the strong vibrational resonance to ethylene. With the B source added in the flame, a shoulder at 10.494 μm on the main absorption peak rises up and is attributed to the BH bending mode (υ_2, a fundamental band at 953.0 cm^{-1}) of BH_2 radicals in the flame, suggesting the generation of BH_2 in the flame (*24*). To resonantly couple the laser energy into BH_2 radicals, a laser beam with a wavelength of 10.494 μm and a bandwidth of 100 kHz, which perfectly matches the BH_2 bending mode, is then selected to irradiate the flame during the BDD deposition process. We used the power difference between the incident laser power and the transmitted power as the absorbed power. Strictly speaking, the power difference includes non-absorption power loss caused by particulate scattering, flame turbulence, and beam steering. However, the large absorption cross section (5 m^2/mol) of ethylene (*25*) and the observed flame shrinkage upon laser irradiation suggest that the effective absorption dominates the laser energy loss as passing the flame.

We prepared BDD films with laser vibrational excitations at different absorbed laser powers for 30 min. As shown in Fig. 3 (A and C), the diamond grain size shows a linear increase as the absorbed laser power increases for the same deposition time. As shown in the Raman spectra (Fig. 3B), the diamond peak increases in intensity and shows a red shift to a higher wave number with an increasing absorbed laser power, suggesting considerable improvement of the diamond quality. The improvement in the diamond quality can be attributed to two factors: enlarged grain size and improved diamond crystallinity. The large-grained films have much less grain boundaries, where defect formation dominates, and therefore exhibit a higher diamond quality. To rule out the grain size effect on the diamond quality enhancement, we prepared BDD films with the same thickness under laser vibrational excitations at different absorbed laser powers by varying the deposition time (section S1 and fig. S1). As shown in fig. S1 (A and B), the average grain sizes of the BDD films with same thicknesses of 8.5 μm are similar and around 5 μm. Although these films have a similar grain size, their Raman spectra (fig. S1C) show that the diamond peak becomes stronger as the absorbed laser power increases. The enhancement of the diamond quality in the BDD films with the same thickness and grain size suggests that the introduction of laser vibrational excitation of

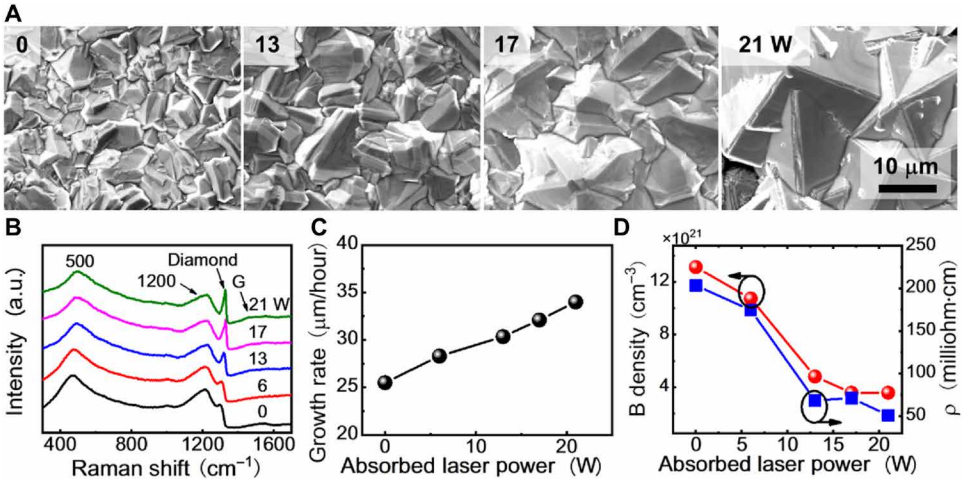

Fig. 3. Growth of BDDs with laser vibrational excitations at different absorbed laser powers. (**A** and **B**) SEM micrographs and Raman spectra of BDDs prepared with laser vibrational excitation of BH_2 at different absorbed laser powers. (**C**) The grain size, (**D**) the B density (red circle), and the film resistivity (blue square) plotted as a function of the absorbed laser power.

the growth critical species, BH_2, plays a critical role in essentially improving the diamond crystallinity by eliminating the defect formation during the grain growth.

Meanwhile, an obvious shift to a higher wave number of the "500 cm^{-1}" band with the absorbed laser power is also noticed. This band can be fitted by the sum of a Gaussian and a Lorentzian component (section S2 and fig. S2), and the wave number of the Lorentzian component exhibits a one-to-one relationship with the B density (*26*)

$$[B]\ \mathrm{cm}^{-3} = 8.44 \times 10^{30} \cdot e^{(-0.048 \times \omega(\mathrm{cm}^{-1}))} \quad (1)$$

where $[B]$ is the density of B atoms in the diamond crystal lattice (cm^{-3}) and ω is the wave number of the Lorentzian component of the 500 cm^{-1} band (cm^{-1}). The B density determined from the Raman spectra shows a decrease with a factor of three from 1.2×10^{22} to 4×10^{21} cm^{-3} as the absorbed laser power increases from 0 to 21 W.

Film resistivity and doping density should be in inverse proportion, but an opposite change in the film resistivity is found. The film resistivity is lower in the BDD film with a lower B density prepared with a high absorbed laser power (Fig. 3D), suggesting that more conductive BDDs are obtained with laser vibrational excitation. Conductivity is a complex physical quantity, and many factors influence charge transport, including grain size, impurity in boundary, and defect structure (*23*). Combined with the surface morphological observation and the diamond quality evaluation, the drop of the film resistivity upon the absorbed laser power could be attributed to the grain size effect and the improved diamond crystallinity. On one side, trapping of charge carriers at the grain boundaries, which negatively influence the carrier transport, is largely eliminated in the large-grained film prepared with laser vibrational excitation of BH_2. On the other side, the carriers in highly crystalline BDD films encounter less defect scattering within the grain; hence, their conduction is much more efficient than in defective diamond films. To understand the influence of diamond crystallinity on the film resistivity, we evaluated the film resistivity of the BDD films with the same thickness of 8.5 μm and found that the BDD films prepared with laser excitations have smaller film resistivity than the one prepared without laser excitation in fig. S1D, confirming the positive role of laser vibrational excitation in preventing diamond crystallinity degradation without sacrificing the conductivity during the in situ B doping. Note that a 8.5-μm-thick BDD film can be prepared in 15 min using the laser-assisted combustion flame with a growth rate of 35 μm/hour, which is 30 to 100 times faster than HFCVD and MPCVD (*4*, *5*, *17*, *18*, *20*, *23*, *27*, *28*).

A comprehensive analysis was carried out on the BDD film prepared with laser vibrational excitation at an absorbed laser power of 21 W. The film resistivity is 28.1 milliohm·cm at 300 K and exhibits a negative temperature dependence (Fig. 4A), which is a typical temperature profile for doped semiconductors. Hall effect measurement shows that the free hole density (Fig. 4B) of the film is 4.0×10^{21} cm^{-3} at 300 K, which matches the secondary ion mass spectrometry (SIMS) result, 4.3×10^{21} cm^{-3} (section S3 and fig. S3), confirming full activation of B in the film. The Hall hole mobility

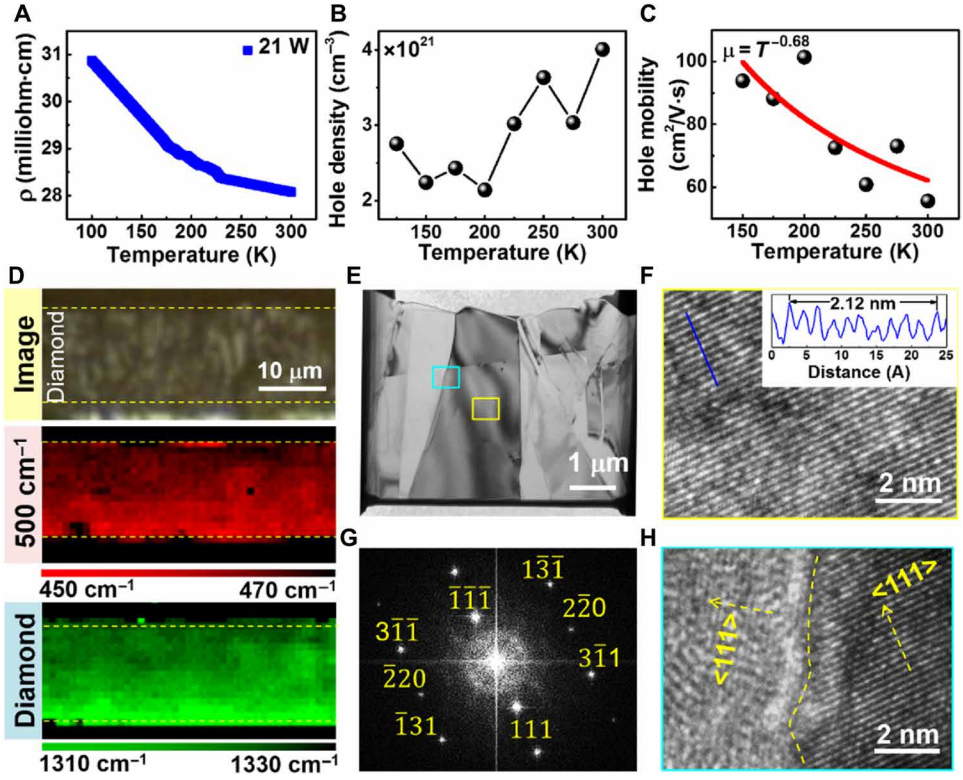

Fig. 4. Characterization of a BDD film prepared with laser vibrational excitation at an absorbed laser power of 21 W. (**A** to **C**) The temperature-dependent film resistivity, Hall hole density, and Hall hole mobility curves. (**D**) Cross-sectional optical image and Raman mapping of the 500-cm^{-1} band position and the diamond peak position. Transmission electron microscopy (TEM) characterization: (**E**) low magnification image, (**F**) HRTEM, and (**G**) fast Fourier transform pattern of the diamond grain marked by the yellow square in (E) and (**H**) high-resolution TEM (HRTEM) of the gain boundary marked by the blue square in (E).

(Fig. 4C) at 300 K was 55.6 $cm^2 V^{-1} s^{-1}$, which is 200 times higher than nanocrystalline diamond films (*22*) and 20 to 70 times higher than polycrystalline diamond films (*5*, *29*, *30*) with similar doping concentrations. Nanocrystalline BDD films normally have small carrier mobility because of the abundant grain boundaries, which impede efficient electrical transport. The possible reason for the larger Hall hole mobility of the BDD samples prepared with laser excitation in this work than the reported polycrystalline BDD films could be the dopants in the BDD prepared with laser excitation that mainly occupy substitutional doping sites, not interstitial doping sites. The fitting line in Fig. 4C corresponds to the best fit of the temperature-dependent mobility using $\mu = T^{-0.68}$. The expected temperature dependence of the mobility for acoustic phonon scattering is $\mu = T^{-3/2}$ and for ionized impurities scattering is $\mu = T^{3/2}$ (*31*). The interpretation of the temperature-dependent mobility indicates that acoustic phonon scattering dominates in the charge transport of BDDs. The low resistivity and the high hole mobility of BDD film prepared with laser vibrational excitation suggests the critical role of good crystallinity in the electrical property.

Raman mapping (Fig. 4D) was performed to evaluate the cross-sectional doping distribution and uniformity of the BDD film prepared with laser vibrational excitation at an absorbed laser power of 21. Both the diamond peak and the 500-cm^{-1} band shift toward a lower wave number along the cross section from the top surface to the bottom film-substrate interface, suggesting that the B density near the surface is lower than beneath. The Raman spectra and the peak position curves versus the depth from the bottom to the top surface measured with a 1-μm interval are provided in section S2 (fig. S2). The linear red shift of the 500-cm^{-1} band position confirms a continuous drop of B density from the film-substrate interface to the top surface. The high doping density at the film-substrate interface is related to high nucleation density, where accumulation of dopants at the grain boundary dominates. The decrease in B density throughout the film could be attributed to continuous diffusion of B from the hot growing surface inward in the film.

Transmission electron microscopy (TEM) was performed to evaluate the atomic-level crystal structure integrity. A TEM sample containing three adjacent diamond grains was extracted from the BDD film prepared at an absorbed laser power of 21 W using the focused ion beam lift-out technique. As shown in the cross-sectional TEM image (Fig. 4E), clear and sharp grain boundaries are identified. The brightness contrast between adjacent grains is due to a large difference in their crystallographic orientation. A high-resolution TEM (HRTEM) image (Fig. 4F) of the diamond grain at the center, marked by a yellow rectangle in Fig. 4E, shows continuous diamond {111} planes, confirming the good diamond grain quality. The radius of a B atom (1.17 Å) is larger than that of a C atom (0.91 Å), and the B—C bond length (1.6 Å) is slightly longer than the C—C bond (1.5 Å). Boron impurity located at the substitutional or interstitial sites would cause an expansion of the diamond lattice. A distance line profile across 10 planes results in an interplane d_{111} value of 2.12 Å, larger than that of an undoped diamond (2.06 Å), suggesting notable lattice expansion upon B doping. The Fourier transform pattern shows that the view direction was along $[11\bar{2}]$ (Fig. 4G). An HRTEM image (Fig. 4H) of the grain boundary, marked by a blue rectangle in Fig. 4E, shows a sharp division between the two adjacent grains with different crystallographic orientations. No amorphous or graphitic carbon phase is found at the diamond grain boundaries. Grain boundaries with nondiamond impurity phase strongly reduce the carrier mobility at high doping levels (*22*). Grain boundary scattering at a sharp boundary free of nondiamond impurities is greatly eliminated, which could explain the high hole mobility obtained in the Hall effect measurement described above.

Electrochemical performance for glucose detection

Conductive BDDs are the subject of considerable interest as an electrode material for electroanalytical applications because of their superior electrochemical properties, including low capacitance background current, wide working potential window, and stable electrochemical activity (*32*–*34*). Glucose is a target molecule for diabetes testing. Using glucose as an organic model, electrochemical tests were carried out to evaluate the performances of the homemade BDD electrodes in glucose sensing and were compared to a commercial planar BDD electrode. As shown in Fig. 5A, the direct glucose oxidation on the BDD surface involves a simple oxidoreduction reaction. Hydroxyl radicals and glucose molecules adsorb on the BDD surface where B active sites are present. Then, oxygen transfer results in the oxidation of glucose to gluconolactone (*34*)

$$\mathrm{BDD} + \mathrm{H_2O} \rightarrow \mathrm{BDD}(^{\bullet}\mathrm{OH}) + \mathrm{H^+} + e^- \quad (2)$$

$$\mathrm{BDD}(^{\bullet}\mathrm{OH}) + \mathrm{BDD(glucose)} \rightarrow \mathrm{BDD} + \mathrm{BDD(gluconolactone)} + \mathrm{H^+} + e^- \quad (3)$$

Figure 5B compares cyclic voltammetry (CV) scans recorded at BDD electrodes prepared with different absorbed laser powers in the presence of 10 mM glucose in 0.1 M sodium hydroxide (NaOH). Glucose oxidation occurs at a potential of 0.7 V [versus silver/silver chloride (Ag/AgCl)]. The peak current of the BDD electrode made from the oxyacetylene flame (termed as homemade BDD below) is twice as high as that of the commercial BDD electrode. The anodic current due to glucose oxidation depends strongly on the doping level and the conductivity of the BDD electrodes (*34*). Although the commercial BDD electrode has a better diamond quality based on Raman and SEM micrographs (section S3 and fig. S3), the high B density (~1.2×10^{22} cm^{-3}) and the low film resistivity (0.2 ohm·cm at 300 K) of the homemade BDD outperform the commercial BDD in glucose electro-oxidation (6.8×10^{20} cm^{-3}, 4616 ohm·cm at 300 K; section S3 and fig. S3).

Although the heavily doped BDD electrode made from the B-added oxyacetylene flame shows its superiority in glucose oxidation, there is still room to improve the performance by enhancing the diamond crystallinity. The introduction of laser vibrational excitation during the BDD growth boosts the electrochemical response of the prepared BDD electrodes for glucose oxidation. As the absorbed laser power increases, the peak current due to glucose oxidation gradually increases (Fig. 5B). Figure 5C presents the steady-state amperometric response of the BDD electrodes at an applied potential of 0.7 V (versus Ag/AgCl) in 0.1 M NaOH after successive additions of glucose. The current response of these BDD electrodes to glucose is enhanced as the absorbed laser power increases, consistent with the CV data. More detail and test results on the glucose electro-oxidation are provided in section S4 (fig. S4). An appreciable enhancement in glucose oxidation and the fact that the BDD electrodes responded to a glucose concentration as low as 0.25 mM suggests the importance of high crystallinity in exploiting full scope performance of BDD-based devices and the advantages

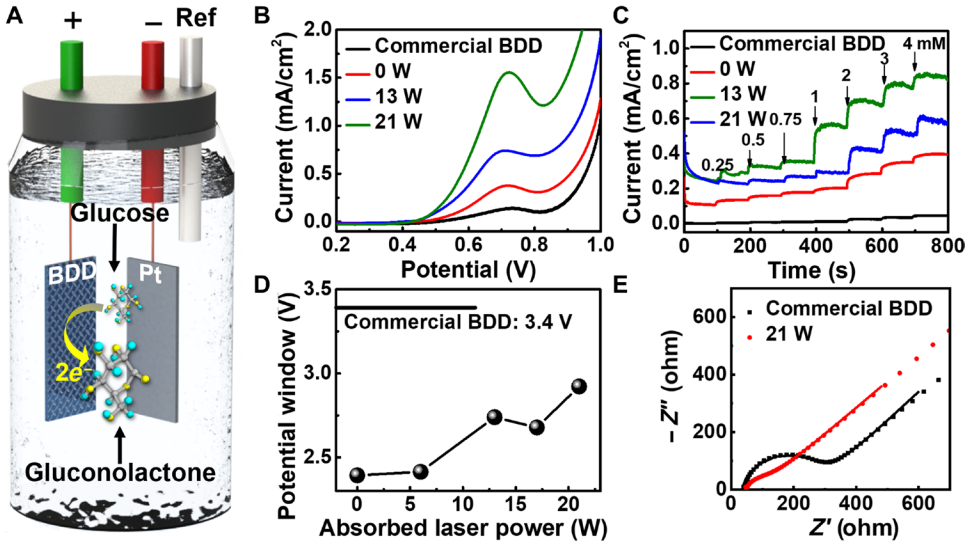

Fig. 5. Electrochemical tests of BDD electrodes. (**A**) Schematic illustration of glucose detection setup. (**B**) CV scans in 10 mM glucose in 0.1 M NaOH. (**C**) Amperometric scans at an applied potential of 0.7 V (versus Ag/AgCl) in 0.1 M NaOH after successively adding glucose with different concentrations. (**D**) Working potential window of a commercial BDD electrode and BDD electrodes prepared with laser vibrational excitation at different absorbed laser powers in 0.1 M sulfuric acid (H_2SO_4). (**E**) Nyquist plots of a commercial BDD electrode and a BDD electrode obtained with laser vibrational excitation at an absorbed laser power of 21 W in 1 M potassium chloride (KCl) with 5 mM potassium ferricyanide $K_3[Fe(CN)_6]$.

of laser vibrational excitation in producing high-performance BDD electrodes.

The working potential of BDD electrodes is directly related to their crystalline quality (*33*). As shown in Fig. 5D, the working potential windows of the homemade BDD electrodes in 0.1 M H_2SO_4 are narrower than the commercial ones (3.4 V) because of the relatively lower crystalline quality. However, it is noticed that the working potential window becomes wider (up to 2.9 V) as the absorbed laser power increases. The widened working potential of the BDD electrodes is related to the improvement of crystallinity quality with the help of laser vibrational excitation of BH_2.

Figure 5E compares the Nyquist plots of the BDD electrode prepared with an absorbed laser power of 21 W and the commercial one in 1 M KCl with 5 mM $K_3[Fe(CN)_6]$. The impedance spectra are fitted using several parameters, including electrolyte resistance (R_s), charge transfer resistance (R_{ct}), a double-layer capacitance (C_{dl}), and Warburg impedance (Z_w); the equivalent circuit is shown in the section S4 (fig. S4). The BDD electrode prepared with an absorbed laser power of 21 W had a lower R_{ct} (85 ohm·cm^2) than the commercial one (270 ohm·cm^2). The small R_{ct} value suggests that the transfer rates of electron are accelerated on the highly conductivity BDD electrode prepared with laser vibrational excitation.

Gas chemistry analysis

Structure/property analysis and the electrochemical tests conclude that laser vibrational excitation plays a critical role in producing highly conductive and crystalline BDDs for high-performance electroanalytical applications. Material growth by CVD is determined by the chemical processes occurring in the gas phase. To understand the growth observations with laser vibrational excitation, the underpinning flame chemistry was fully analyzed using optical emission spectroscopy (OES) and laser-induced fluorescence (LIF). Spatially resolved flame emission images in Fig. 6A with laser vibrational excitation at different absorbed laser powers provide us with insight into the radical distribution within the flame. The flame becomes brighter and shorter as the absorbed laser power increased, suggesting that the combustion reaction is accelerated and more active radicals are generated. The emission peaks from three main species (C_2, CH, and BH) are detected in OES spectra in the wavelength range of 400 to 460 nm (Fig. 6B): (i) C_2: $A^3\Pi_g \rightarrow X^3\Pi_u$, (ii) CH: $A^2\Delta \rightarrow X^2\Pi$, and (iii) BH: $A^1\Pi \rightarrow X^1\Sigma^+$. All emission peaks from the detectable radicals rise as the absorbed laser power increases, confirming that laser vibrational excitation stimulated their generation. OES can only probe excited-state radicals, whose population in the reacting system is several orders of magnitude smaller than the ground-state ones. To compensate for the limitation of OES, LIF was performed to evaluate the abundance of ground-state radicals in the flame. The LIF signals of C_2 ($A \rightarrow X$ (1,1)) at 512.9 nm, CH ($A \rightarrow X$ (0,0)) at 434.4 nm, and BH ($A \rightarrow X$ (1,1)) at 431.6 nm were separately observed (section S5 and fig. S5).

The relative abundance of the radicals in the flame is evaluated by integrating their peaks in the OES and LIF spectra and plotted as a function of the absorbed laser power in Fig. 6 (C and E). The integrated peak intensities for both excited- and ground-state species (i.e., C_2, CH, and BH) in the flame increase as absorbed laser power increases, suggesting that more excited- and ground-state species are generated under laser resonant excitations.

To figure out why more active species are generated in the flame under laser excitations, the flame temperature, T_{flame}, is analyzed at different absorbed laser powers. The detailed calculation procedure is illustrated in the section S6 (fig. S6). The flame temperature is found to increase by 400 K as the absorbed laser power increases to 21 W (Fig. 6D). The rise in flame temperature suggests that laser energy initially absorbed in the vibrational modes is redistributed to the external modes, thus accelerating chemical reactions. Gas-phase combustion is a complex process, involving chemical reactions and interactions of large amount of active species, among which carbon-based species play important roles in the diamond deposition. The

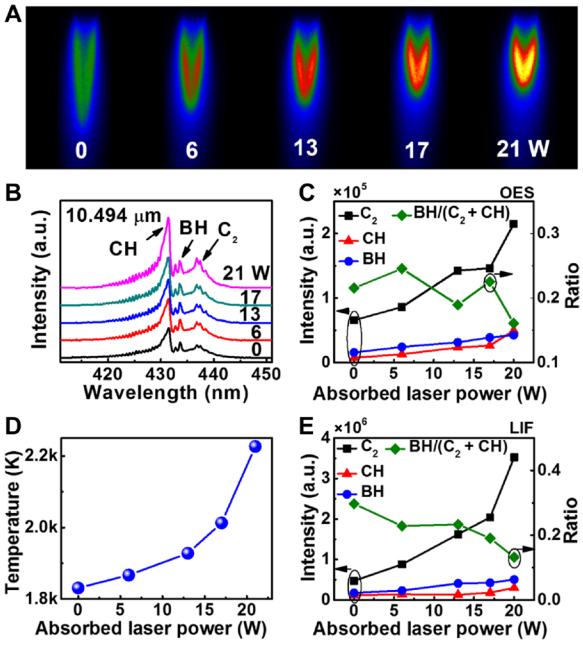

Fig. 6. Optical diagnostics of the B-added oxyacetylene flame. (**A**) The natural emission images of the combustion flame with laser vibrational excitation at different absorbed laser powers. (**B**) OES spectra of the combustion flame with laser vibrational excitation at different absorbed laser powers. (**C** and **E**) The integrated intensity of OES and LIF peaks of different species and the ratio BH/(C_2 + CH) plotted as a function of the absorbed laser power. (**D**) Flame temperature plotted as a function of the absorbed laser power.

OES study revealed an obvious enhancement of emission intensity from C_2 and CH with laser resonant excitation of ethylene. Matsui *et al.* (*35*) reported a strong dependence of the diamond deposition rate on the C_2 concentration profile. CH has been viewed as the basic building block for diamond nucleation in CVD (*36*). The accelerated generation of C_2 and CH in the flame under the laser excitation is crucial in promoting the overall deposition rate as shown in Fig. 3C. Since all the species reflected by the OES peaks rise up upon the laser excitation, the absolute integrated peak intensities of species are not proper to be used for extracting the decisive species influencing the diamond crystallization.

The relative ratio between BH and the sum of the CH and C_2 radicals drops as the laser power absorbed increases. The downshift of the relative ratio between BH and C_2 + CH upon laser power absorption indicates that the laser vibrational excitation process does not serve simply as a conventional heating source. The active laser control through vibrationally exciting BH_2 causes the reactants to preferentially follow one of many different reaction routes in a thermal nonequilibrium way that the generation of C_2 and CH is promoted more than BH; in other words, the relative abundance of BH to hydrocarbons is effectively suppressed.

The observed enhancement in the growth rate and the crystallinity of BDD films with the introduction of laser vibrational excitation of BH_2 is probably related to the preferential suppression of the relative ratio between BH and C_2 + CH in the flame. An in-depth understanding of the role of BH in the doping and crystallization processes is necessary to correlate the flame chemistry with the observations in BDD growth. Boron hydride plays a double-edged role in BDD growth (*34*, *37*). As analogs to CH_x insertion to a diamond surface, BH_x can attach to a vacant site using a B—H bond with a further attachment of carbon radicals (*38*). Boron hydride is, therefore, a major species causing B incorporation in the diamond lattice due to its small insertion energy (*38*). Meanwhile, the formation of excessive BH and rapid interconversion among the various BH_x species (BH, BH_2, and BH_3) through the "H-shifting reactions" leads to concomitant H atom loss in the reacting system and a bad C:H ratio that causes a transition from faceted to unfaceted morphology (*34*, *39*).

Hydrogen atoms play a fundamental role in creating active nucleation sites for diamond crystallization and preferentially etch-unwanted sp^2-bonded carbon, thus eliminating nondiamond carbon codeposition (*40*). The depletion of H atoms due to the formation of boron hydrides hinders the etch of unwanted sp^2-bonded carbon and results in codeposition of graphitic carbon, explaining the onset of graphitization observed in high-level doping BDD growth. The laser vibrational excitation of BH_2 suppresses the relative ratio of BH to carbon-containing species (C_2 and CH), confirming the detrimental role of excess BH in affecting the crystallinity. The detrimental role of excessive BH in degrading diamond crystallinity is also confirmed in the OES study of the flame chemistry at different B flow rates (section S7 and fig. S7). The fundamental mechanism of B doping in diamond lattice is not completely understood, which hinders the control on B doping and, thereby, the realization of functionality that needs to be yet explored. With the discovery of powerful laser vibrational control, it is now possible to obtain a more clear-cut idea of how to design and execute previously unidentified doping schemes.

DISCUSSION

Laser control of reactions at the microscopic level is one of the hot research areas. It is well established in chemical physics but less explored in practical applications, although pivotal promise toward scientific breakthroughs is envisioned. We developed a laser vibrational excitation route to modify the reacting chemistry and achieved highly conductive and crystalline BDDs for glucose sensing. The combined features of a fast growth rate, high crystallinity, and conductivity strengthen the competitiveness of BDDs as the next generation of electrochemical devices. Semiconductor doping in a well-controlled manner is a prerequisite for achieving defined property modification and realizing designed functions of solid-state devices. It plays a crucial role in sustaining the development of industries, such as microelectronics, optoelectronics, sensing, and energy storage. The discovery of the effective roles of laser vibrational excitation in regaining diamond crystallinity in the doping process is of great significance for improving the growth quality and doping flexibility of a broad range of technically important semiconductors, thus holding the promise of removing the long-standing bottlenecks in the semiconductor-based microelectronics industry.

MATERIALS AND METHODS

Growth of BDD electrodes

BDDs were prepared using laser-assisted combustion diamond CVD, as shown in Fig. 1. The p-type silicon (Si) wafers were used as substrates. The substrates were ultrasonically seeded in a 5-nm diamond slurry. A combustion flame generated from a mixture of acetylene and oxygen with flow rates of 1685 and 1795 sccm, respectively, was used. Boron was introduced by bubbling a third acetylene line through a boric oxide methanol solution (10 g/liter). Boric acid was

purchased from Sigma-Aldrich. The flow rate of the B source carried by the acetylene was tuned from 0 to 100 sccm to control the doping density in the diamond films. A wavelength-tunable, continuous-wave carbon dioxide (CO_2) laser (9.2 to 10.9 μm; PRC Inc.) was used as the irradiation source. The laser beam was focused to ~2 mm in diameter to cover the inner core of the oxyacetylene flame. A power meter was placed in the laser path next to the combustion flame for laser energy absorption measurement. The substrates were placed on a water-cooled three-axis moving state and brought to the proximity of the flame inner core during the deposition. The substrate temperature was controlled by tuning the cooling water rate and was kept at 780° ±10°C during the deposition.

Characterization

Surface morphologies of the samples were performed on a field-emission SEM (FESEM) (5 kV; Hitachi S-4700 FESEM system). TEM observations were performed on a field-emission TEM (200 kV; FEI Tecnai Osiris). Chemical structures were evaluated using a micro-Raman spectrometer (inVia, Renishaw). The resistivity was measured using a homemade electrical property measurement system consisting of a semiconductor parameter analyzer (Agilent 4155C) and a probe station (Cascade Microtech, MPS 150). The Hall effect measurement was conducted in a Quantum Design Physical Property Measurement System (PPMS) using an external Keithley 2400 source meter and standard lock-in technique. Doping concentration was evaluated by collaborators from Institut de Chimie de la Matière Condensée de Bordeaux (ICMBC) in France using a SIMS (TOF.SIMS 5, IONTOF Inc.) with O_2 ions (2 keV, area of 300 μm by 300 μm).

Electrochemical tests

An electrochemical processing grade, free-standing BDD was purchased from Element Six Inc. and used as receive. The specification of the commercial BDD was as follows: polycrystalline, size, 5.0 mm by 5.0 mm; thickness, 0.45 mm; and boron concentration range, 2 to 6 × 10^{20}/cm^3. All chemicals used in the electrochemical tests were purchased from Sigma-Aldrich and used as received. These were D-(+)-glucose (> 99.5%), H_2SO_4, $K_3[Fe(CN)_6]$, and NaOH (>97%). All solutions were made from deionized water of resistivity not less than 18.2 megohm·cm at 298 K (Millipore UHQ). For electrochemical oxidation of glucose, a standard 0.1 M NaOH solution was used. All electrochemical tests were measured using an electrochemical workstation (CHI760, CH Instruments Inc.). The as-deposited BDD samples were polished by sandpaper to eliminate SiO_2 for connection purpose. A circular, chemically stable rubber ring with an area of 0.1 mm^2 was attached to the BDD film to confine the interaction area. The rest of the sample surface was covered by a nonconductive, chemically stable J-B Weld glue. A standard three-electrode configuration was used, consisting of a BDD working electrode, a platinum cage counter electrode, and an Ag/AgCl reference electrode. All BDD working electrodes were prepared with the same surface area, 2 mm^2. Before each electrochemical oxidation test, 10 repetitive CV scans of the BDD electrodes in 0.1 M NaOH were performed to electrochemically activate the surface. Magnetic stirring at the bottom of the electrochemical cell was used to enhance the mass transport process.

Optical diagnostics of flame chemistry

A detailed illustration of the OES and LIF of the combustion flame is provided in section S8 (fig. S8). All measurements were performed using an optical spectrometer (three gratings: 150, 600, and 2400 lines/mm; range: 190 to 800 nm; Andor Technology) equipped with an intensified charge-coupled device. The following data acquisition parameters were fixed: a gate delay of 0 μs, a gate width of 10 μm, and a grating of 600 lines/mm. Spectra and optical images were taken with a horizontal slit width of 50 and 2500 μm, respectively. The high-resolution spectra for rotational temperature measurements were collected with a horizontal slit width of 5-μm centered at the flame inner core and a grating of 2400 lines/mm.

SUPPLEMENTARY MATERIALS

Supplementary material for this article is available at http://advances.sciencemag.org/cgi/content/full/7/4/eabc7547/DC1

REFERENCES AND NOTES

1. H. Schmid, M. T. Björk, J. Knoch, S. Karg, H. Riel, W. Riess, Doping limits of grown in situ doped silicon nanowires using phosphine. *Nano Lett.* **9**, 173–177 (2009).
2. J. Jeon, T. Asano, Y. Shimura, W. Takeuchi, M. Kurosawa, M. Sakashita, O. Nakatsuka, S. Zaima, Effect of in situ Sb doping on crystalline and electrical characterizations of n-type $Ge_{1-x}Sn_x$ epitaxial layer. *Jpn. J. Appl. Phys.* **55**, 04EB13 (2016).
3. J. H. Comfort, R. Reif, Plasma-enhanced chemical vapor deposition of in situ doped epitaxial silicon at low temperatures. II. Boron doping. *J. Appl. Phys.* **65**, 1067–1073 (1989).
4. R. Ramamurti, M. Becker, T. Schuelke, T. Grotjohn, D. Reinhard, G. Swain, J. Asmussen, Boron doped diamond deposited by microwave plasma-assisted CVD at low and high pressures. *Diam. Relat. Mater.* **17**, 481–485 (2008).
5. L. Li, H. Li, X. Lü, S. Cheng, Q. Wang, S. Ren, J. Liu, G. Zou, Dependence of reaction pressure on deposition and properties of boron-doped freestanding diamond films. *Appl. Surf. Sci.* **256**, 1764–1768 (2010).
6. N. E. Henriksen, Laser control of chemical reactions. *Chem. Soc. Rev.* **31**, 37–42 (2002).
7. R. N. Zare, Laser control of chemical reactions. *Science* **279**, 1875–1879 (1998).
8. F. F. Crim, Chemistry. Making energy count. *Science* **316**, 1707–1708 (2007).
9. S. Yan, Y.-T. Wu, B. Zhang, X.-F. Yue, K. Liu, Do vibrational excitations of CHD_3 preferentially promote reactivity toward the chlorine atom? *Science* **316**, 1723–1726 (2007).
10. X. de Hemptinne, D. de Keuster, Mode selective laser chemistry of ethylene. *J. Chem. Phys.* **73**, 3170–3177 (1980).
11. L. S. Fan, Y. S. Zhou, M. X. Wang, Y. Gao, L. Liu, J. F. Silvain, Y. F. Lu, Resonant vibrational excitation of ethylene molecules in laser-assisted diamond deposition. *Laser Phys. Lett.* **11**, 076002 (2014).
12. L. S. Fan, Z. Q. Xie, J. B. Park, X. N. He, Y. S. Zhou, L. Jiang, Y. F. Lu, Synthesis of nitrogen-doped diamond films using vibrational excitation of ammonia molecules in laser-assisted combustion flames. *J. Laser Appl.* **24**, 022001 (2012).
13. L.-S. Fan, L. Constantin, D.-w. Li, L. Liu, K. Keramatnejad, C. Azina, X. Huang, H. R. Golgir, Y. Lu, Z. Ahmadi, F. Wang, J. Shield, B. Cui, J.-F. Silvain, Y.-F. Lu, Ultraviolet laser photolysis of hydrocarbons for nondiamond carbon suppression in chemical vapor deposition of diamond films. *Light Sci. Appl.* **7**, 17177 (2018).
14. H. R. Golgir, Y. Gao, Y. S. Zhou, L. S. Fan, P. Thirugnanam, K. Keramatnejad, L. Jiang, J.-F. Silvain, Y. F. Lu, Low-temperature growth of crystalline gallium nitride films using vibrational excitation of ammonia molecules in laser-assisted metalorganic chemical vapor deposition. *Cryst. Growth Des.* **14**, 6248–6253 (2014).
15. S. J. Cobb, Z. J. Ayres, J. V. Macpherson, Boron doped diamond: A designer electrode material for the twenty-first century. *Annu. Rev. Anal. Chem.* **11**, 463–484 (2018).
16. V. V. S. S. Srikanth, P. S. Kumar, V. B. Kumar, A brief review on the in situ synthesis of boron-doped diamond thin films. *Int. J. Electrochem.* **2012**, 218393 (2012).
17. K. Miyata, K. Kumagai, K. Nishimura, K. Kobashi, Morphology of heavily B-doped diamond films. *J. Mater. Res.* **8**, 2845–2857 (1993).
18. E. Gheeraert, A. Deneuville, J. Mambou, Influence of diborane on the growth rate and phase stability of diamond films. *Carbon* **37**, 107–111 (1999).
19. Y. Zou, K. Larsson, Effect of boron doping on the CVD growth rate of diamond. *J. Phys. Chem. C* **120**, 10658–10666 (2016).
20. P. Hartmann, S. Bohr, R. Haubner, B. Lux, P. Wurzinger, M. Griesser, A. Bergmaier, G. Dollinger, H. Sternschulte, R. Sauer, Diamond growth with boron addition. *Int. J. Refract. Metals Hard Mater.* **16**, 223–232 (1998).
21. Y. G. Wang, S. P. Lau, B. K. Tay, X. H. Zhang, Resonant Raman scattering studies of Fano-type interference in boron doped diamond. *J. Appl. Phys.* **92**, 7253–7256 (2002).
22. W. Gajewski, P. Achatz, O. A. Williams, K. Haenen, E. Bustarret, M. Stutzmann, J. A. Garrido, Electronic and optical properties of boron-doped nanocrystalline diamond films. *Phys. Rev. B* **79**, 045206 (2009).

23. P. Ashcheulov, J. Šebera, A. Kovalenko, V. Petrák, F. Fendrych, M. Nesládek, A. Taylor, Z. V. Živcová, O. Frank, L. Kavan, M. Dračínský, P. Hubík, J. Vacík, I. Kraus, I. Kratochvílová, Conductivity of boron-doped polycrystalline diamond films: Influence of specific boron defects. *Eur. Phys. J. B* **86**, 443 (2013).
24. F. X. Sunahori, M. Gharaibeh, D. J. Clouthier, R. Tarroni, BH2 revisited: New, extensive measurements of laser-induced fluorescence transitions and ab initio calculations of near-spectroscopic accuracy. *J. Chem. Phys.* **142**, 174302 (2015).
25. C. L. Strand, Y. Ding, S. E. Johnson, R. K. Hanson, Measurement of the mid-infrared absorption spectra of ethylene (C_2H_4) and other molecules at high temperatures and pressures. *J. Quant. Spectrosc. Radiat. Transf.* **222-223**, 122–129 (2019).
26. F. Brunet, P. Germi, M. Pernet, Microstructural study of boron doped diamond films by x-ray diffraction profiles analysis. *Thin Solid Films* **322**, 143–147 (1998).
27. G. M. Swain, R. Ramesham, The electrochemical activity of boron-doped polycrystalline diamond thin film electrodes. *Anal. Chem.* **65**, 345–351 (1993).
28. M. Bernard, A. Deneuville, P. Muret, Non-destructive determination of the boron concentration of heavily doped metallic diamond thin films from Raman spectroscopy. *Diam. Relat. Mater.* **13**, 282–286 (2004).
29. J. Mort, K. Okumura, M. Machonkin, Charge transport in boron-doped diamond thin films. *Philos. Mag. B* **63**, 1031–1036 (1991).
30. R. J. Zhang, S. T. Lee, Y. W. Lam, Characterization of heavily boron-doped diamond films. *Diam. Relat. Mater.* **5**, 1288–1294 (1996).
31. S. M. Sze, K. K. Ng, *Physics of Semiconductor Devices* (John Wiley & Sons Inc., 2007).
32. K. Muzyka, J. Sun, T. H. Fereja, Y. Lan, W. Zhang, G. Xu, Boron-doped diamond: Current progress and challenges in view of electroanalytical applications. *Anal. Methods* **11**, 397–414 (2019).
33. D. Luo, L. Wu, J. Zhi, Fabrication of boron-doped diamond nanorod forest electrodes and their application in nonenzymatic amperometric glucose biosensing. *ACS Nano* **3**, 2121–2128 (2009).
34. Z. Deng, H. Long, Q. Wei, Z. Yu, B. Zhou, Y. Wang, L. Zhang, S. Li, L. Ma, Y. Xie, J. Min, High-performance non-enzymatic glucose sensor based on nickel-microcrystalline graphite-boron doped diamond complex electrode. *Sens. Actuat. B Chem.* **242**, 825–834 (2017).
35. Y. Matsui, A. Yuuki, M. Sahara, Y. Hirose, Flame structure and diamond growth mechanism of acetylene torch. *Jpn. J. Appl. Phys.* **28**, 1718–1724 (1989).
36. F. G. Celii, J. E. Butler, Diamond chemical vapor deposition. *Annu. Rev. Phys. Chem.* **42**, 643–684 (1991).
37. D. W. Comerford, A. Cheesman, T. P. F. Carpenter, D. M. E. Davies, N. A. Fox, R. S. Sage, J. A. Smith, M. N. R. Ashfold, Y. A. Mankelevich, Experimental and modeling studies of B atom number density distributions in hot filament activated B_2H_6/H_2 and $B_2H_6/CH_4/H_2$ gas mixtures. *J. Phys. Chem. A* **110**, 2868–2875 (2006).
38. Z. M. Shah, A. Mainwood, A theoretical study of the effect of nitrogen, boron and phosphorus impurities on the growth and morphology of diamond surfaces. *Diam. Relat. Mater.* **17**, 1307–1310 (2008).
39. Q. Liang, J. G. Harrison, Y. K. Vohra, Modeling of nitrogen/diborane/methane/hydrogen plasma for nanocrystalline diamond growth: Comparison with experimental data. *Diam. Relat. Mater.* **17**, 2067–2070 (2008).
40. R. Haubner, S. Bohr, B. Lux, Comparison of P, N and B additions during CVD diamond deposition. *Diam. Relat. Mater.* **8**, 171–178 (1999).

Acknowledgments

Funding: The authors appreciate the financial support from NSF (CMMI 1826392) and Nebraska Center for Energy Sciences Research (NCESR). **Author contributions:** The work was completed through contributions of all authors. All authors have given approval to the final version of the manuscript. The individual contributions are as follows: supervision and conceptualization, Y.F.L.; manuscript writing, L.F.; synthesis, L.C., L.F., and Z.P.W.; electrochemical test, L.F., Z.P.W., K.A.M., T.H., C.D.-C., R.Y.L., and X.L.; electrical transport characterization, X.G.C.; TEM characterization, F.W. and B.C.; and dopant characterization, J.F.S. **Competing interests:** The authors declare that they have no competing interests. **Data and materials availability:** All data needed to evaluate the conclusions in the paper are present in the paper and/or the Supplementary Materials. The datasets generated during the current study are available from the corresponding author on reasonable request. Additional data related to this paper may be requested from the authors.

Submitted 12 May 2020
Accepted 2 December 2020
Published 20 January 2021
10.1126/sciadv.abc7547

Citation: L. Fan, L. Constantin, Z. P. Wu, K. A. McElveen, X. G. Chen, T. He, F. Wang, C. Debiemme-Chouvy, B. Cui, R. Y. Lai, X. Li, J. F. Silvain, Y. F. Lu, Laser vibrational excitation of radicals to prevent crystallinity degradation caused by boron doping in diamond. *Sci. Adv.* **7**, eabc7547 (2021).

Science Advances

Laser vibrational excitation of radicals to prevent crystallinity degradation caused by boron doping in diamond

L. Fan, L. Constantin, Z. P. Wu, K. A. McElveen, X. G. Chen, T. He, F. Wang, C. Debiemme-Chouvy, B. Cui, R. Y. Lai, X. Li, J. F. Silvain and Y. F. Lu

Sci Adv **7** (4), eabc7547.
DOI: 10.1126/sciadv.abc7547